Acta Astronautica 222 (2024) 493–507

Contents lists available at ScienceDirect

Acta Astronautica

journal homepage: www.elsevier.com/locate/actaastro

Research Paper

Multi-disciplinary optimization of single-stage hybrid rockets for lunar ascent

Paolo Maria Zolla [*,1], Rodrigo Rosa [2], Mario Tindaro Migliorino [3], Daniele Bianchi [4]

Sapienza University of Rome, Via Eudossiana 18, 00184, Rome, Italy

ARTICLE INFO

Keywords:
Hybrid rocket engines
Multi-disciplinary optimization
Lunar ascent
Space propulsion

ABSTRACT

This study aims to determine the optimal design and ascent trajectory for a single-stage hybrid rocket in the context of a lunar ascent mission, with the objective of reaching a 100 km circular orbit on the Moon equatorial plane. A multi-disciplinary optimization problem is formulated, integrating flight design variables and launch vehicle design variables to achieve the best mission scenario. A zero-dimensional internal ballistics model is employed to estimate key parameters such as thrust, mass flow rate, and gross mass of the hybrid rocket, while a three-degree of freedom dynamical model is utilized to simulate the ascent trajectory. The resulting integrated optimization problem is solved using an in-house heuristic algorithm that combines particle swarm and genetic algorithms. Two propellant combinations, liquid oxygen/paraffin-wax and hydrogen peroxide (90%)/high-density polyethylene, are evaluated, considering both their performance in the integrated system and the feasibility of the proposed mission. After conducting a sensitivity analysis to investigate the influence of particle count in the optimization process, results for both propellant combinations are presented. While paraffin and oxygen provide the highest payload ratio, hydrogen peroxide and polyethylene entail a more feasible and flexible design for a lunar mission.

1. Introduction

A hybrid rocket motor (HRM) employs a combination of a liquid or gaseous oxidizer and a solid fuel as propellants. Usually, the combustion chamber houses a solid fuel grain, while the oxidizer is injected through a feed system. Compared to liquid rocket engines, hybrid rockets offer a higher volumetric specific impulse, while maintaining lower complexity and costs due to the presence of a single feeding system. With respect to solid rocket motors, they provide a higher specific impulse and the flexibility of throttling and restart capabilities. Furthermore, hybrid rockets employ environmentally friendly, non-toxic propellants, and the separation of oxidizer and fuel increases the safety of the propulsion system. Due to these advantages, there is a growing interest in utilizing HRMs for specific propulsion applications, such as main engines for suborbital vehicles [1,2], or as upper stages in multi-stage rockets [3,4]. The typical layout of a HRM is depicted in Fig. 1.

Additionally, hybrid rockets have gained significant interest for extraterrestrial missions, especially in the context of outer planet exploration [5–7] and lunar applications [8,9]. In particular, significant efforts are presently engaged towards the development of the lunar orbital platform gateway (LOP-G) [10]. The LOP-G will not only facilitate deep space missions but also validate technologies for lunar surface missions and pave the way for future Mars missions [9]. Thus, for efficient transfers between the surface of the moon and the LOP-G, the development of optimized propulsion systems is of paramount importance, and hybrid rockets emerge as promising candidates for this purpose [9].

When optimizing hybrid rockets, it is essential to consider the interplay between the unique combustion physics of hybrid rockets, characterized by mixture ratio shifts, and the generation of an adequate thrust, which is significantly influenced by the motor design and can impact the ascent trajectory. Therefore, an integrated optimization approach is required to maximize the overall performance of the launch vehicle (LV). In line with this approach, previous studies such as [4,11–15] have focused on the design optimization of a hybrid upper stage for a VEGA-based launcher. In [1,16], the optimization of a single-stage hybrid rocket-powered vehicle for suborbital flight is explored. Ref. [17] presents a robust design optimization for a three-stage hybrid rocket launcher. Lastly, in [18], the optimization of a single-stage

* Corresponding author.
E-mail addresses: paolomaria.zolla@uniroma1.it (P.M. Zolla), rosa.1937948@studenti.uniroma1.it (R. Rosa), mariotindaro.migliorino@uniroma1.it (M.T. Migliorino), daniele.bianchi@uniroma1.it (D. Bianchi).
[1] Ph.D. student, Department of Mechanical and Aerospace Engineering.
[2] M.Sc. student, Department of Mechanical and Aerospace Engineering.
[3] Research Assistant Professor, Department of Mechanical and Aerospace Engineering.
[4] Associate Professor, Department of Mechanical and Aerospace Engineering.

https://doi.org/10.1016/j.actaastro.2024.06.026
Received 19 March 2024; Received in revised form 17 May 2024; Accepted 15 June 2024
Available online 19 June 2024
0094-5765/

Symbols

A	Area (m^2)
a	Pre-exponential factor (mm/s (m^2s/kg)^n)
a_x	Axial acceleration (m/s^2)
C_{bed}	Catalyst capacity (kg/(m^3s))
C_F	Thrust coefficient (–)
c^*	Characteristic velocity (m/s)
D	Diameter (m)
F	Thrust (N)
$\boldsymbol{g}$	Gravitational acceleration vector (m/s^2)
g_0	Earth gravitational acceleration (m/s^2)
h	Altitude (m)
I_{sp}	Specific impulse (s)
I_{vol}	Volumetric specific impulse (s (kg/m^3))
k_s	Structural coefficient (–)
L	Length (m)
m	Mass (kg)
$\dot{m}$	Mass flow rate (kg/s)
n	Mass flux coefficient (–)
O/F	Mixture ratio (–)
p	Pressure (bar)
R	Gas constant (J/(kg K))
$\boldsymbol{r}$	Vehicle position vector (m)
$\dot{r}$	Fuel regression rate (mm/s)
S	Lateral surface (m^2)
$\dot{s}$	Erosion rate (mm/s)
t	Time (s)
t_b	Burning Time (s)
T	Temperature (K)
V	Volume (m^3)
v	Vehicle velocity (m/s)
$\boldsymbol{v}$	Vehicle velocity vector (m/s)
λ	Payload ratio (–)
γ	Specific heat ratio (–)
δ	Thickness (m)
η	Efficiency –
ε	Nozzle area ratio (–)
ρ	Density (kg/m^3)
θ	Elevation (rad)
ψ	Azimuth (rad)
σ	Material yield strength (MPa)
ξ	BLT curvature (–)

Subscripts

0	Initial design parameter value
a	Air
anc	Ancillaries
bed	Catalytic bed
blt	Bi-linear tangent
c	Chamber
co	Coasting
cont	Contingencies
e	Exit
f	Final value
feed	Feeding system
fu	Fuel
g	Grain
gas	Pressurant gas
h	Head
i	Initial value
ins	Thermal insulation
LO	Lift-off
max	Maximum
noz	Nozzle
orb	Orbital injection
ox	Oxidizer
p	Port
PO	Pitch-over
prop	Propellant
ref	Reference
s	Structure
sh	Shrouds
t	Throat
tk	Tank
u	Payload
vac	Vacuum
$\mathcal{R}$	Radial-transverse-normal reference frame
$\mathcal{T}$	Topocentric reference frame

Acronyms

BLT	Bi-Linear Tangent
GA	Genetic Algorithm
HDPE	High-Density PolyEthylene
HHA	Hybrid Heuristic Algorithm
HRM	Hybrid Rocket Motor
LLO	Low Lunar Orbit
LOP-G	Lunar Orbital Platform-Gateway
LOX	Liquid Oxygen
LRE	Liquid Rocket Engine
PSO	Particle Swarm Optimization
SRM	Solid Rocket Motor
LV	Launch Vehicle
PO	Pitch-Over

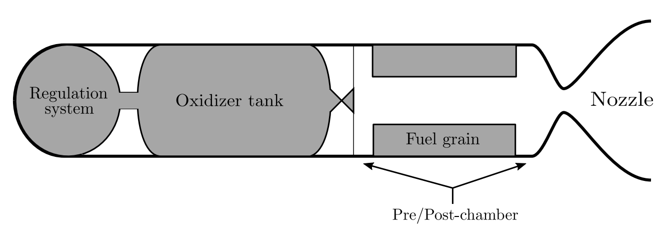

Fig. 1. Typical hybrid rocket layout.

LOX/Wax hybrid rocket with swirl injection for a lunar ascent mission is presented.

This paper presents a comprehensive analysis of a multi-disciplinary optimization problem for a lunar ascent mission to a 100 km circular orbit. This altitude, representing the upper limit for low lunar orbits (LLO), has been selected due to the significance of LLOs in lunar exploration. Additionally, LLOs can serve as intermediate orbits for transfers to the Lunar Gateway. The analysis employs a single-stage hybrid rocket to demonstrate the viability of this propulsion system.

The study focuses on evaluating two propellant combinations: liquid oxygen (LOX)/paraffin-wax ($C_{32}H_{66}$) and 90% hydrogen peroxide (H_2O_2)/high-density polyethylene (HDPE). The trade-off between these propellant combinations considers various factors, including their performance, the impact of mixture ratio shifts, effects on structural efficiency, and feasibility within the proposed mission scenario. Despite having a relatively low regression rate due to its pyrolizing nature, the use of HDPE is feasible in the current application due to the low thrust requirements resulting from the Moon small gravitational pull. The evaluation provides valuable insights into the selection of optimal propellant combinations for achieving the desired mission objectives.

This work is organized as follows. Section 2 presents the internal ballistics model used to evaluate the HRM propulsive performance 2.1 and structural mass 2.2, followed by a comprehensive overview of the two propellant combinations examined in this study 2.3. The mathematical model of the ascent trajectory is discussed in Section 3, pointing out the considered launch vehicle dynamics 3.1, the flight strategy 3.2, the constraints 3.3, and all flight parameters considered as design variables 3.4. Section 4 presents the in-house algorithm used to solve the integrated optimization problem analyzed in this paper 4.1, followed by a detailed description of the cost function used 4.2. Numerical results of the multi-disciplinary optimization are presented in Section 5.

2. Hybrid rocket model

This section presents the modeling of the HRM internal ballistics (hereinafter referred to as "HRM model") that will be coupled to the flight dynamics in the multi-disciplinary optimization problem. The internal ballistics computations are first presented, followed by the estimation of the structural mass, and by a general evaluation of the propellants considered.

2.1. Internal ballistics

A zero-dimensional quasi-steady approach is employed [19], with properties of the gases inside the combustion chamber assumed uniform in space. This allows the reduction of the computational effort required to compute the performance parameters necessary to the flight dynamics model, namely thrust and mass flow rate over time, and gross mass. Efficient computations are crucial in optimization loops, as it is required to run HRM calculations a large number of times.

In the present work, LOX/Wax and H_2O_2(90%)/HDPE are evaluated as the propellant combinations. The fuel is stored in the combustion chamber as a single-port cylindrical solid grain, while the oxidizer is stored in a tank as a liquid. Since the thrust-to-weight ratio required for a lunar ascent mission is relatively low, there is no need for complex grain geometries such as the multi-perforated grain [20].

The fuel grain shape is uniquely defined by its external diameter, D_c, initial port diameter, $D_{p,0}$ (the subscript "0" refers to values at the start of the HRM burn), and length, L_g, where $D_{p,0}$ and L_g are inputs of the HRM model, while D_c is an output. Following [21], a simple relation between the head-end pressure and chamber pressure is used to account for total pressure losses along the grain:

$$p_h = p_c(1 + 0.5\Gamma^2 J^2) \tag{1}$$

where $\Gamma = \sqrt{\gamma\left(\frac{2}{\gamma+1}\right)^{\frac{\gamma+1}{\gamma-1}}}$, γ is the combustion products specific heat ratio, and $J = A_t/A_p$ is the ratio of throat area over port area. To guarantee limited pressure losses and greater legitimacy of a 0-D model, the value of the throat-to-port area ratio, J, at ignition is constrained to be lower than 0.5, which results in a low Mach number in the combustion chamber (at least < 0.3).

The oxidizer is injected with a pressure-fed regulated system into the combustion chamber. Hence, with this feeding system, the oxidizer mass flow rate is not constant with time and depends on the difference between the tank and head pressure. Following [3], assuming turbulent and incompressible flow, the oxidizer mass flow rate can be computed with:

$$\dot{m}_{ox} = \sqrt{\frac{p_{tk} - p_h}{Z}} \tag{2}$$

where Z is the hydraulic resistance in the oxidizer flow path, set according to the value of the oxidizer mass flow rate at ignition, $\dot{m}_{ox,0}$, which is an input of the model. The tank pressure, kept constant using an evaporated propellant regulation system, is assumed to be $p_{tk} = 2.5p_{h,0}$ for LOX and $p_{tk} = 3.5p_{h,0}$ for H_2O_2. Since the hybrid rocket analyzed in this work must operate on the Moon where there is no atmosphere, a pressure-fed system seems an appropriate choice to reduce complexity and costs without significantly affecting performance.

The injection of the oxidizer in the combustion chamber is assumed to occur with a non-zero tangential component of velocity (i.e., swirl injection). This approach leads to an enhancement of convective heat exchange and regression rates [22–24]. Swirl injection has been shown to improve the nominal regression rate of paraffin-based hybrid rockets by up to 2.4 times compared to axial injection. Furthermore, the introduction of a tangential component enhances propellant mixing even in the absence of a post-chamber, enabling combustion efficiency values of up to 99% [25]. Lastly, experimental evidence presented in [22] has confirmed that the use of a pre-chamber does not provide any benefits for swirl injection, contributing instead to a loss of flow momentum. Consequently, by reducing the required chamber length, a more compact design can be achieved, effectively addressing one of the primary challenges associated with hybrid rocket propulsion, which can be characterized by high length-to-diameter ratios [15].

The fuel regression rate is assumed uniform along the grain port, neglecting the contributions of the lateral ends. Its value is assumed to be dependent only on the instantaneous oxidizer mass flux:

$$\dot{r} = aG_{ox}^n \tag{3}$$

where $\dot{r}$ is expressed in mm/s, the oxidizer mass flux, $G_{ox} = \dot{m}_{ox}/A_p$, in $\mathrm{kg/(m^2s)}$, and n is the mass flux coefficient, equal to 0.62 for LOX/Wax [26] and 0.5 for H_2O_2(90%)/HDPE [25,27–30]. The enhancement in regression rate resulting from the use of swirl injection is considered. However, for the current application, there is a lack of established literature data for a suitable correlation between the pre-exponential factor, a, and the geometric swirl number, which is characteristic of the motor design. Consequently, assuming that the swirl number can be tailored to meet the required regression rate, the value of a (which is an input parameter) can be optimized within the range of $0.13 - 0.3\ \mathrm{mm/s} \cdot (\mathrm{m^2s/kg})^n$ for LOX/Wax [22,26], and $0.016 - 0.09\ \mathrm{mm/s} \cdot (\mathrm{m^2s/kg})^n$ for H_2O_2(90%)/HDPE [25]. The fuel mass flow rate coming from the grain can therefore be evaluated as:

$$\dot{m}_{fu} = \rho_{fu}\dot{r}L_g\pi D_p \tag{4}$$

Once the oxidizer and fuel mass flow rates are known, the mixture ratio, $\mathrm{O/F} = \dot{m}_{ox}/\dot{m}_{fu}$, and total mass flow rate, $\dot{m}_e = \dot{m}_{ox} + \dot{m}_{fu}$, can be computed. Assuming an isentropic expansion in a choked nozzle, the chamber pressure is obtained as:

$$p_c = \frac{\dot{m}_e c^*}{A_t} \tag{5}$$

The NASA Chemical Equilibrium with Applications software (CEA [31]) is used to obtain the data on the propellants' characteristic velocity and specific heat ratio. The conservative assumption of frozen flow expansion in the nozzle is employed to compute the characteristic velocity. The specific heat ratio is taken at the combustion chamber condition. Data are interpolated with a shape-preserving piecewise cubic function for both chamber pressure and oxidizer-to-fuel ratio:

$$c^* = \eta_{c^*} c^*_{CEA}\left(p_c, \mathrm{O/F}\right) \tag{6}$$

$$\gamma = \gamma_{CEA}\left(p_c, \mathrm{O/F}\right) \tag{7}$$

Losses in the nozzle expansion, mixing, and combustion are taken into account assuming a 98% nozzle efficiency, $\eta_{C_F} = 0.98$, and c^* efficiency, $\eta_{c^*} = 0.98$.

The thrust coefficient, C_F, is computed assuming a 1-D isentropic expansion to the exit pressure, p_e, with a constant specific heat ratio, γ, in a vacuum environment:

$$C_F = \eta_{C_F}\left(\Gamma\sqrt{\frac{2\gamma}{\gamma-1}\left[1-\left(\frac{p_e}{p_c}\right)^{\frac{\gamma-1}{\gamma}}\right]}+\varepsilon\frac{p_e}{p_c}\right) \tag{8}$$

$$F = \dot{m}_e c^* C_F \tag{9}$$

where ε is the nozzle area ratio. Since the hybrid rocket operates on the Moon, ambient pressure effects on thrust are neglected. The nozzle geometry is identified by the throat diameter, $D_{t,0}$, and area ratio, ε_0, at ignition, both inputs of the HRM model.

Nozzle throat erosion is taken into account according to [32]:

$$\dot{s} = \left(\frac{\dot{s}_0}{0.0001}\right)\left(\frac{0.025}{D_t}\right)^{0.2}\left[6.4392\times10^{-5}\Phi^{-1.991}\cdot \cdot\exp\left(\frac{-3.1082}{\Phi}+1.84\right)p_c^{0.0535\Phi^2-0.2641\Phi+1.0365}\right] \tag{10}$$

where $\Phi = \frac{\mathrm{O/F}}{\mathrm{O/F_{st}}}$, the subscript "st" refers to stoichiometric conditions, and $\dot{s}_0$ is the reference erosion rate of the propellant combination, equal to 0.1 and 0.07 mm/s for LOX/Wax and H_2O_2(90%)/HDPE, respectively, according to [33]. Notice that the erosion rate (here expressed in mm/s and with p_c in bar) depends on chamber pressure and mixture ratio, accounting for both the intensity of the throat heat flux and for the oxidizing species concentration in the exhaust gases [32,34].

Port and throat radii are updated in time according to the modeled regression and erosion rates. Iterations stop once a target burning time, t_b, which is an input of the model, has been reached. The grain external diameter, D_c (coincident with the case inner diameter), is computed as the value required to host the fuel used during the burn plus residual contingencies equal to 3% (accounting for fuel sliver). In order to design a compact rocket, the nozzle exit diameter, $D_e = D_{t,0}\sqrt{\varepsilon_0}$, is enforced to be lower or equal than the case diameter, D_c. Please note that the nozzle exit diameter, D_e, is considered reasonably unaffected by the erosion process.

A thorough validation of the presented internal ballistics model can be found in [19].

2.2. Structural mass estimation

The structural mass of the different subsystems is taken into account according to [35,36]. In particular, the combustion chamber mass can be computed by summing the mass of the cylindrical case with the mass of a 2.5 cm - thick injector plate:

$$m_c = 0.025\rho_c\pi\left(\frac{D_c}{2}\right)^2 + \rho_c\pi D_c L_c\delta_c \tag{11}$$

where ρ_c is the combustion chamber and injector plate material density, L_c is the combustion chamber length, and δ_c its thickness, computed using Mariotte's formula for pressurized cylinders with a 1.5 safety factor:

$$\delta_c = 1.5\frac{p_{h,max}D_c}{2\sigma_c} \tag{12}$$

where σ_c is the maximum yield strength of the case material and $p_{h,max}$ is the maximum head pressure over the HRM burn. In this work, the combustion chamber is assumed to be made of 7050 aluminum alloy, while the oxidizer tank of carbon fiber composite with an epoxy resin matrix (see Table 1). The length of the combustion chamber is assumed equal to the grain length $L_c = L_g$ since, according to [22,25], pre- and post-chamber are not necessarily required in a swirl-injected configuration.

The oxidizer tank is assumed to have a cylindrical shape with two ellipsoidal domes, and a 5% initial volume ullage is reserved for the pressurizing gas. Tank thickness can be computed with Eq. (12), as performed for the combustion chamber. The total oxidizer mass stored in the tank is computed by integrating the oxidizer mass flow rate over time plus 3% contingencies:

$$m_{ox} = 1.03\int_0^{t_b}\dot{m}_{ox}(t)\,\mathrm{d}t \tag{13}$$

When utilizing liquid oxygen, it is crucial to consider tank insulation. Specifically, the empirical formula provided in [37] has been employed to estimate the required mass for insulating the oxidizer tank:

$$m_{ins} = 1.123S_l \tag{14}$$

where S_l is the lateral surface to be insulated, expressed in m^2. The mass related to covering exposed sections of the rocket has been taken into account according to the following empirical formula [37]:

$$m_{sh} = 4.95S_{sh}^{1.15} \tag{15}$$

where S_{sh} (in m^2, subscript "sh" for shrouds) is the lateral surface to be covered. Shrouded sections of the rocket include the ellipsoidal domes of the tank. As the rocket must operate on the Moon, the presence of a heat shield for the payload has not been considered.

Following [35], the nozzle mass is estimated using an empirical model for phenolic nozzles, where the mass is proportional to the initial expansion ratio, ε_0, and the total propellant exhausted, m_{prop} (in kg), by using:

$$m_{noz} = 125\left(\frac{m_{prop}}{5400}\right)^{2/3}\left(\frac{\varepsilon_0}{10}\right)^{1/4} \tag{16}$$

The nozzle is assumed to be made of a conical convergent section with a 45 degrees half-angle, plus a bell-shaped divergent section. Its total length can be estimated as follows:

$$L_{noz} = \frac{D_c - D_{t,0}}{2\tan(\pi/4)} + 0.8\frac{D_e - D_{t,0}}{2\tan(\pi/12)} \tag{17}$$

where the divergent bell length is assumed 80% that of a conical divergent with a 15 degrees half-angle.

When using hydrogen peroxide, a catalytic bed is necessary to ensure its decomposition into oxygen and water vapor. The use of a catalytic bed eliminates the need for an igniter, as products of decomposition of hydrogen peroxide show hypergolic properties with many fuels, making it particularly suitable for restartable systems. However, it is important to consider the weight of the catalytic bed as it contributes to the overall mass budget of the HRM.

According to [38], experimental evidence has shown that for a specific class of catalytic beds (characterized primarily by feed pressure and mass flow rate), the catalyst capacity, C_{bed}, can be considered constant. This quantity, which represents the decomposable propellant per unit of volume of the catalyst, can be written as follows:

$$C_{bed} = \frac{\dot{m}_{ox}}{V_{bed}} \tag{18}$$

where V_{bed} is the required volume of the catalyst to achieve full decomposition of $\dot{m}_{ox}$. For the current application, due to the extremely similar operating conditions with respect to the configuration presented in [39], a reference conservative value of catalyst capacity $C_{bed} = 245$ kg/(m^3s) has been considered. To ensure sufficient residence time for complete decomposition, the length of the HRM catalyst is assumed to be equal to $L_{bed} = 0.1\dot{m}_{ox}$ [39], while its thickness, δ_{bed}, can be computed according to Eq. (12) considering a maximum pressure equal to the tank pressure, p_{tk}. Therefore, the catalyst bed mass, m_{bed}, can be easily computed as:

$$m_{bed} = \rho_{bed}L_{bed}\frac{\pi}{4}\left[\left(D_{bed}+\delta_{bed}\right)^2 - D_{bed}^2\right] \tag{19}$$

The catalyst bed is assumed to be made of INCONEL 718. Density and maximum yield strength of the materials for the combustion chamber,

Table 1
Density, ρ and maximum yield strength, σ, of the combustion chamber, oxidizer tank, and catalyst bed materials.

Subsystem	ρ [kg/m^3]	σ [MPa]	Material
Combustion chamber	2800	300	Aluminum Alloy 7050 [40]
Oxidizer tank	1600	600	Carbon fiber composite with epoxy resin [41]
Catalyst bed	8190	900	INCONEL 718 [42]

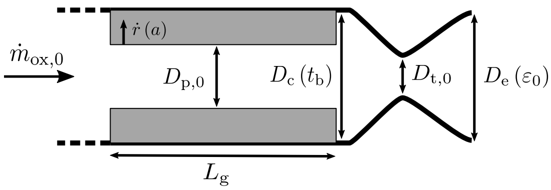

Fig. 2. Hybrid rocket design parameters.

oxidizer tank, and catalyst bed are listed in Table 1. Given the limited availability of simple relationships in literature, the pressure drop across the catalyst is accounted for by increasing the pressure in the tank from $p_{tk} = 2.5p_{h,0}$ for LOX to $p_{tk} = 3.5p_{h,0}$ for H_2O_2.

Regulated tank pressurization is achieved using evaporated propellant. In the case of liquid oxygen, part of the liquid oxidizer passes through a heater and is reinserted into the tank in order to keep its pressure constant. On the other hand, in the case of H_2O_2, decomposed gases are spilled from the catalytic bed and used for the same purpose. The pressurizing gases are thermally insulated from the liquid oxidizer through a diaphragm. The total oxidizer mass necessary for tank pressurization can be estimated using the ideal gases equation of state:

$$m_{gas} = \frac{p_{tk} V_{ox}}{R_{gas} T_{tk}} \tag{20}$$

where R_{gas} is the pressurizing gas constant (about 260 J/(kg · K) for gaseous oxygen and 124 J/(kg · K) for decomposed hydrogen peroxide), V_{ox} is the oxidizer volume to pressurize, and T_{tk} is the ullage temperature (200 K for gaseous oxygen and 650 K for decomposed hydrogen peroxide). It must be underlined that the extra tank mass necessary to host the oxidizer used as pressurizing gas is taken into account.

Lastly, mass and length of ancillaries structures (such as piping) is assumed to be 10% of the total mass and length of the HRM [36]. To summarize, a set of 7 input parameters (referred to as $\boldsymbol{x}_{HRM}$) uniquely defines a hybrid rocket design and operating condition for which, using the HRM model, the performance metrics, mass budget, and dimensions can be computed:

$$\boldsymbol{x}_{HRM} = [L_g, D_{p,0}, D_{t,0}, \varepsilon_0, \dot{m}_{ox,0}, a, t_b] \tag{21}$$

A schematic description of the hybrid rocket design is shown in Fig. 2.

2.3. Propellant combinations

Two propellant combinations have been considered for the discussed mission, namely LOX/Wax, to prioritize performance, and H_2O_2(90%)/HDPE, to prioritize mission feasibility. In order to make a proper choice, multiple factors have to be considered, such as their theoretical performance, the effects of mixture ratio variations, structural efficiency, and compatibility with the proposed mission.

In terms of performance, liquid oxygen exhibits a higher peak vacuum specific impulse, as expected. Specifically, at a chamber pressure of 5 bar and a reference expansion ratio equal to 30, values that are close to what will be obtained as a result of the optimization process, oxygen achieves a peak specific impulse of 329 s (+2.8%) compared to the 320 s offered by hydrogen peroxide, as depicted in Fig. 3(a). The vacuum specific impulse has been computed analytically as $I_{sp} = c^* C_F / g_0$, with c^* and γ computed using the CEA software as per Eqs. (6) and (7), and C_F computed with Eq. (8), as in Section 2. It must be underlined that the computed I_{sp} is the theoretical one, assuming both η_{C_F} and η_{c^*} equal to 1. Note that the optimal mixture ratio ensuring maximum theoretical performance is lower than what one might expect due to the conservative assumption of frozen flow from the combustion chamber and due to the small chamber pressure of 5 bar used for the computations.

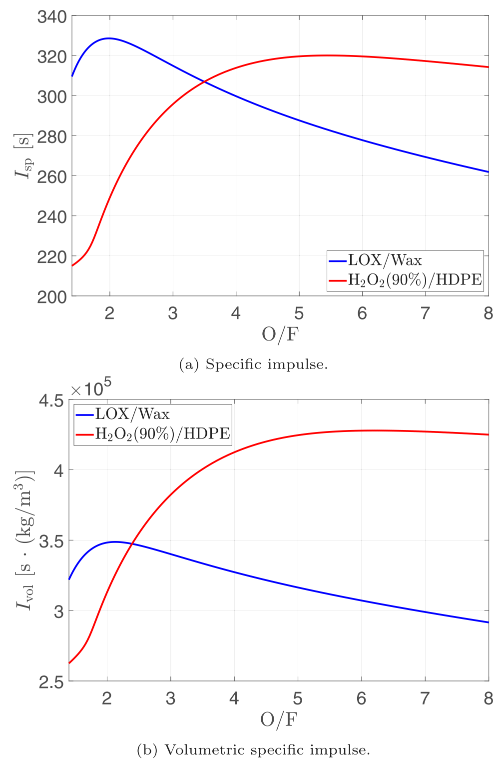

Fig. 3. Comparison between LOX/Wax and H_2O_2(90%)/HDPE theoretical performance metrics.

In hybrid rockets, the mixture ratio is affected by the time evolution of the port diameter and of the oxidizer mass flow rate. In fact, rearranging Eqs. (3) and (4) yields:

$$\mathrm{O/F} \propto \dot{m}_{ox}^{1-n} D_p^{2n-1} \tag{22}$$

In the case of LOX (mass flux coefficient $n > 0.5$) the mixture ratio is expected to increase during operations at constant $\dot{m}_{ox}$ due to the regression of the fuel grain. Conversely, with $n = 0.5$, the choice of hydrogen peroxide eliminates the dependency of the mixture ratio on the port diameter. Hence, O/F can be kept around the optimal value, maximizing I_{sp}. Although the oxidizer mass flow rate still has an influence on O/F, its impact is less significant given its slower variation compared to D_p.

Therefore, when choosing LOX, it is expected that operating within the relatively narrow band of O/F yielding maximum specific impulse (Fig. 3(a)) cannot be satisfied throughout the whole HRM burn. On the other hand, hydrogen peroxide provides a flatter curve and is hence more robust to O/F shifts.

Table 2
Oxidizer, ρ_{ox}, and fuel, ρ_{fu}, densities for LOX/Wax and H_2O_2(90%)/HDPE.

	ρ_{ox} [kg/m^3]	ρ_{fu} [kg/m^3]
LOX/Wax	1140	900
H_2O_2(90%)/HDPE	1400	970

Another metric that is useful to take into account is the volumetric specific impulse (Fig. 3(b)), defined as the product between the specific impulse and the average propellant density:

$$I_{vol} = I_{sp}\frac{\rho_{ox}O/F + \rho_{fu}}{O/F + 1} \tag{23}$$

It is evident that the H_2O_2(90%)/HDPE propellant combination has the highest volumetric specific impulse due to the significantly higher average density and optimal mixture ratio, compared to LOX/Wax. This leads to improved structural efficiency, as the propellants require less storage space. Indeed, the higher densities of hydrogen peroxide and HDPE compared to both LOX and paraffin-wax, lead to the design of more volumetrically efficient combustion chamber and oxidizer tank. Oxidizer and fuel densities for each propellant combination are listed in Table 2.

When considering hydrogen peroxide, it has to be taken into account its easier storability compared to a cryogenic propellant such as LOX. Moreover, the hypergolic properties of decomposed hydrogen peroxide with HDPE simplify motor reignition. Regarding the fuel choice, HDPE offers better mechanical properties with respect to pure paraffin-wax, ensuring grain integrity during engine operations. Lastly, from a numerical point of view, having HDPE as fuel is also important to test the adaptability of the optimizer, given its substantial difference in regression rate with respect to paraffin. Such variation allows us to test the optimizer across a wide spectrum of ballistic parameters.

3. Flight trajectory model

This section provides an overview of the ascent trajectory model used to assess the flight performance of the single-stage lunar ascent vehicle under analysis. The equations of motion are introduced, followed by the adopted flight strategy. Mission constraints are briefly discussed before formulating the integrated optimization problem.

3.1. Dynamical model

The launch vehicle (LV) trajectory analysis is conducted using a three-dimensional three-degrees of freedom (3-DoF) point-mass model. Since there is no atmosphere on the Moon, the degrees of freedom related to the orientation of the rocket can be disregarded. Under this hypothesis, the LV is assumed aligned with the velocity vector. The state of the rocket at any given time can be described by its position vector, $\boldsymbol{r}$, velocity vector, $\boldsymbol{v}$, and mass, m. The equations of motion in an inertial reference frame can be expressed as follows:

$$\dot{\boldsymbol{r}} = \boldsymbol{v} \tag{24}$$

$$\dot{\boldsymbol{v}} = \boldsymbol{g} + \frac{\boldsymbol{F}}{m} \tag{25}$$

$$\dot{m} = -\dot{m}_e \tag{26}$$

Atmospheric drag is neglected, and the gravitational acceleration vector is represented assuming a spherical model for the Moon:

$$\boldsymbol{g} = -\frac{\mu}{r^3}\boldsymbol{r} \tag{27}$$

where μ is the Moon gravitational constant. The absolute value of the thrust force, F, generated by the LV is the vacuum thrust provided by the HRM model. Its direction, $\hat{\boldsymbol{F}}$, which must be optimized since it affects the LV trajectory, is instead controlled by thrust vector control (TVC) actuators.

In the early stages of the ascent trajectory, it is preferable to use a topocentric reference frame $\mathcal{F}_\mathcal{T} = (\hat{\boldsymbol{i}}, \hat{\boldsymbol{j}}, \hat{\boldsymbol{k}})$ (see Fig. 4(a)), fixed on the launch base, to express the thrust direction:

$$\hat{\boldsymbol{F}} = \sin\theta_\mathcal{T}\,\hat{\boldsymbol{i}} + \cos\theta_\mathcal{T}\sin\psi_\mathcal{T}\,\hat{\boldsymbol{j}} + \cos\theta_\mathcal{T}\cos\psi_\mathcal{T}\,\hat{\boldsymbol{k}} \tag{28}$$

where $\theta_\mathcal{T}$ and $\psi_\mathcal{T}$ indicate the thrust elevation and azimuth angles in this frame.

On the other hand, when enough distance has been put between the hybrid rocket and the launch base, the use of a radial-transverse-normal (RTN) local reference frame $\mathcal{F}_\mathcal{R} = (\hat{\boldsymbol{r}}, \hat{\boldsymbol{t}}, \hat{\boldsymbol{n}})$ (Fig. 4(b)) is more appropriate, with the thrust direction that can be expressed as:

$$\hat{\boldsymbol{F}} = \sin\theta_\mathcal{R}\,\hat{\boldsymbol{r}} + \cos\theta_\mathcal{R}\cos\psi_\mathcal{R}\,\hat{\boldsymbol{t}} + \cos\theta_\mathcal{R}\sin\psi_\mathcal{R}\,\hat{\boldsymbol{n}} \tag{29}$$

The TVC actuation angle can be computed as the angular difference between the velocity vector and thrust vector, expressed in the same reference frame.

3.2. Flight strategy

The ascent trajectory is divided into multiple phases based on previous lunar ascent studies [43,44]. Each phase is characterized by a specific control law governing the thrust direction.

The initial phase is a vertical ascent, where the thrust is aligned with the LV velocity to minimize gravitational losses. The thrust direction is set to $\theta_\mathcal{T} = \frac{\pi}{2}$. The duration of this lift-off phase, denoted as t_{LO}, is dependent on the stand-off distance between the LV and the launch base, h_{LO}, which is a parameter to be optimized. Subsequently, a *pitch-over* maneuver is executed, involving a controlled rotation of the nozzle to align the LV with the desired orbital plane. The thrust elevation angle, $\theta_\mathcal{T}$, follows a simple linear decrease, while the azimuth angle, ψ_{PO}, remains constant:

$$\theta_\mathcal{T}(t) = \frac{\pi}{2} + \frac{\theta_{PO} - \pi/2}{t_{PO}}\left(t - t_{LO}\right) \tag{30}$$

where t_{PO} is the duration of the pitch-over phase and θ_{PO} is the kick angle. Once a suitable altitude is reached, the thrust direction can be optimized without significant impact on gravitational losses. During this phase, the elevation angle is controlled using a *bi-linear tangent* (BLT) guidance approach [45], aiming to place the LV into a Hohmann-like transfer orbit. The pitch program in this phase can be described as follows:

$$\theta_\mathcal{R} = \arctan\left(\frac{k^\xi\tan\left(\theta_{blt,i}\right)}{k^\xi + \left(1-k^\xi\right)\tau} + \frac{\left[\tan\left(\theta_{blt,f}\right) - k^\xi\tan\left(\theta_{blt,i}\right)\right]\tau}{k^\xi + \left(1-k^\xi\right)\tau}\right) \tag{31}$$

$$\tau = \frac{t - t_{blt,i}}{t_{blt,f} - t_{blt,i}} \in [0,\ 1] \tag{32}$$

where ξ is a measure of the elevation angle curvature (k^ξ), $t_{blt,i}$ and $t_{blt,f}$ are the starting and ending times of the BLT guidance, $\theta_{blt,i}$ and $\theta_{blt,f}$ are the starting and ending elevation angles, and k is an assigned constant which must be greater than 1 (100 in this analysis). The azimuth angle, ψ_{blt}, is supposed constant during the whole phase. Finally, following a coasting phase of duration t_{co}, a second burn is executed with a constant thrust elevation angle, θ_{orb}, and azimuth angle, ψ_{orb}, to achieve orbit circularization. It is important to note that the inclusion of a coasting phase is made possible by the restart capabilities of hybrid rockets.

To take into account the presence of a second HRM burn, the parameter $\dot{m}_{ox,2}$ is added to the set of inputs $\boldsymbol{x}_{HRM}$ in Eq. (21) (which now includes 8 design variables). A schematic representation of the flight strategy is provided in Fig. 5.

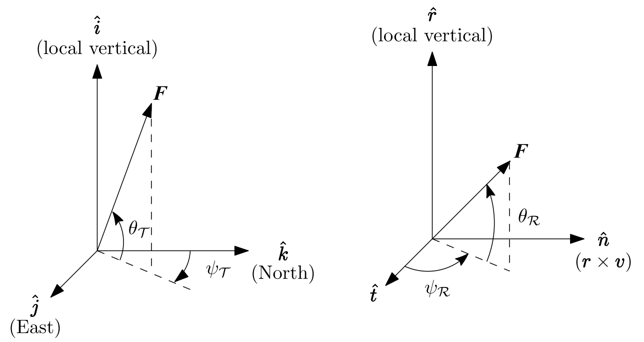

(a) Topocentric reference frame. (b) Radial-traverse-normal reference frame.

Fig. 4. Reference frames.

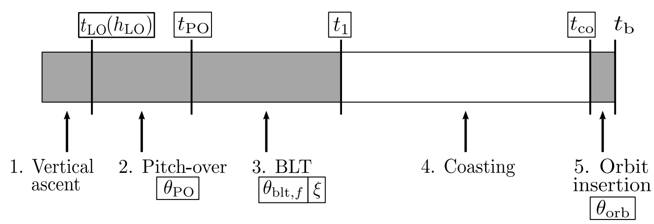

Fig. 5. Phases of the optimal control problem.

3.3. Constraints

The launch vehicle initial conditions are influenced by the geographical location of the launch pad. Specifically, $\boldsymbol{r}_0$ represents the position of the base, while $\boldsymbol{v}_0 = \boldsymbol{\omega} \times \boldsymbol{r}_0$ denotes the initial inertial velocity, with $\boldsymbol{\omega}$ denoting the angular velocity of the Moon rotation. The initial mass of the LV, m_0, is determined by the hybrid rocket mass obtained from the HRM model with specified $\boldsymbol{x}_{\mathrm{HRM}}$, in addition to the payload weight, m_{u}, which is fixed to 500 kg.

Terminal constraints are utilized to ensure payload injection into a circular orbit with desired radius and inclination. Specifically, tolerances of $\delta h = 50\,\mathrm{m}$ and $\delta v = 10\,\mathrm{m/s}$ are enforced for altitude deviation $\Delta h = |h - h_{\mathrm{obj}}|$ and velocity deviation $\Delta v = |v - v_{\mathrm{obj}}|$, respectively. Constraints on the terminal velocity direction are also applied, including in-plane local angle deviation, $\Delta\theta = |\hat{r} \cdot \hat{v} - \theta_{\mathrm{obj}}|$, and out-of-plane inertial angle deviation, $\Delta i = |\hat{v} \cdot \hat{z} - i_{\mathrm{obj}}|$ (where $\hat{z}$ represents the direction of the Moon rotation axis), with tolerances of $\delta\theta = 0.8\,\mathrm{deg}$ and $\delta i = 0.01\,\mathrm{deg}$, respectively. The right ascension of the ascending node, however, is not directly enforced, as it can be easily adjusted to the desired value by carefully selecting the launch time.

To maintain the structural integrity of the launch vehicle and payload throughout the ascent trajectory, the maximum axial acceleration, $a_x = \dot{\boldsymbol{v}} \cdot \hat{\boldsymbol{F}}/g_0$, is limited to 5 g and verified *a posteriori*. Since there is no atmosphere, other path constraints such as maximum dynamic pressure, max-Qα, and payload heat-flux exposure can be disregarded. Lastly, no constraint is enforced on the maximum TVC actuation angle.

3.4. Optimization

In order to find out the maximum payload ratio that can be carried into the desired target orbit, a multi-disciplinary optimization problem is formulated. For the sake of simplicity, the launch pad is assumed to be located at a general point on the equator, with the launch performed in the direction of the Moon rotation.

In addition to the design parameters $\boldsymbol{x}_{\mathrm{HRM}}$ that define the single-stage hybrid rocket, there are other quantities related to flight mechanics and thrust direction that need to be optimized. These are represented by a separate set of parameters denoted as $\boldsymbol{x}_{\mathrm{flight}}$, which govern the trajectory of the launch vehicle. In terms of flight mechanics, the optimization includes determining the vertical ascent stand-off distance, h_{LO}, the duration of the pitch-over phase, t_{PO}, the coasting time, t_{co}, and the duration of the first HRM burn, t_1. It is worth noting that the duration of the second burn can be easily calculated as $t_2 = t_{\mathrm{b}} - t_1$.

The parameters associated with the guidance aspect of the optimization problem are the angles necessary to characterize the thrust direction of the launch vehicle. These angles include the elevation angle at the end of the pitch-over phase, θ_{PO}, the elevation angle at the end of the BLT phase, $\theta_{\mathrm{blt},f}$, along with its curvature, ξ, and the elevation angle during the final orbital injection, θ_{orb}. It is important to note that, given the assumption of an equatorial launch towards an equatorial target orbit, the azimuth angle remains constant throughout the trajectory and can be disregarded in the optimization problem, as it consistently remains at 90 degrees in a topocentric reference frame and 0 degrees in a RTN reference frame. The resulting trajectory is therefore two-dimensional (2-D).

To summarize, the trajectory of the launch vehicle for a given hybrid rocket design (described by $\boldsymbol{x}_{\mathrm{HRM}}$) is uniquely defined by a set of 8 parameters:

$$\boldsymbol{x}_{\mathrm{flight}} = [h_{\mathrm{LO}}, \theta_{\mathrm{PO}}, t_{\mathrm{PO}}, \theta_{\mathrm{blt},f}, \xi, t_1, t_{\mathrm{co}}, \theta_{\mathrm{orb}}] \tag{33}$$

The optimization problem involves the simultaneous optimization of the 8 parameters $\boldsymbol{x}_{\mathrm{HRM}}$ (see Eq. (21)) that describe the design of the hybrid rocket, and the 8 parameters $\boldsymbol{x}_{\mathrm{flight}}$ (Eq. (33)) that define the trajectory. In each iteration of the optimization process, the HRM model is first used to compute the thrust and mass flow rate over time for the first burn. The values of the port diameter, D_{p}, throat diameter, D_{t}, and expansion ratio, ε, at time t_1 are then utilized as inputs for the second burn, which has a duration of $t_{\mathrm{b}} - t_1$ and an oxidizer mass flow rate of $\dot{m}_{\mathrm{ox},2}$. The structural mass of the hybrid rocket is determined for the condition of maximum load. Throttling is assumed to be achieved by adjusting the tank pressure between the two burns through the evaporated propellant regulation system. Once the thrust curve, mass flow rate curve, and gross mass of the hybrid rocket have been calculated, the trajectory analysis can be performed.

4. Optimization strategy

This section presents the optimization strategy adopted for the examined multi-disciplinary problem. In particular, the algorithm used will be presented first, followed by details about the chosen cost function.

4.1. Algorithm

The multi-disciplinary optimization problem at hand is solved using an in-house hybrid heuristic algorithm (HHA) called "PSOGA" (Particle Swarm Optimization with Genetic Algorithm), which combines the well-known algorithms particle swarm optimization (PSO) and genetic algorithm (GA). Heuristic methods are applicable to various optimization problems as they do not rely on explicit assumptions about the function or its gradient [46]. These methods are particularly useful when a more computationally expensive optimization algorithm is not feasible or when the problem exhibits highly non-linear behavior, making gradient-based methods inefficient in finding global optima. Given the characteristics of the lunar ascent mission studied in this paper, heuristic algorithms are considered suitable for the analysis.

In the literature, numerous examples exist where PSO is integrated with GA to form hybrid heuristic algorithms [47–49]. This approach is widely recognized for its effectiveness since PSO accelerates convergence by simulating flying behaviors. However, it has the drawback of potentially getting trapped in local minima. GA mitigates this issue by promoting population diversity, thereby achieving more comprehensive coverage of the design space. Ref. [48] demonstrates that HEAs successfully balance global exploitation and local exploration, outperforming both PSO and GA when tackling complex optimization problems.

The in-house approach employed in this study utilizes two separate populations, each initialized randomly and consisting of the same number of individuals. These populations interact and exchange information to improve the overall solution quality and to reduce computational time. Each individual, represented by a unique set of inputs $\boldsymbol{x} = [\boldsymbol{x}_{\mathrm{HRM}}, \boldsymbol{x}_{\mathrm{flight}}]$, is evaluated using a cost function $f(\boldsymbol{x})$ to determine its movements within the search domain, aiming to minimize the objective function.

The first population in the PSOGA algorithm follows a modified PSO approach, specifically the aging leader variant [50,51], with some adjustments. Each particle update is determined by three velocity components: i) an inertial velocity, $\boldsymbol{v}_{\mathrm{in}}$, that maintains the particle previous direction, ii) a cognitive velocity, $\boldsymbol{v}_{\mathrm{c}}$, that pulls the particle towards its best-known position, and (iii) a social velocity that directs the particle towards the overall best-known position (leader, $\boldsymbol{v}_{\mathrm{s}}$). Each velocity component is multiplied by a random number between 0 and 1.

The PSO swarm is divided into three subgroups: $\mathcal{S}_1$ and $\mathcal{S}_2$, each comprising 10% of the PSO population, and $\mathcal{S}_3$, which includes the remaining 80%. The leader of the first subgroup is the best position found among the GA population ($\boldsymbol{x}_{\mathrm{best,GA}}$), the leader of the second subgroup is the best position found among the PSO particles ($\boldsymbol{x}_{\mathrm{best,PSO}}$), and the leader of the third subgroup is the overall best-known position found by any particle ($\boldsymbol{x}_{\mathrm{best}}$).

If the swarm fails to improve its position for four consecutive iterations, two challengers ($\boldsymbol{x}_{\mathrm{ch},1}$, $\boldsymbol{x}_{\mathrm{ch},2}$) are created, and two subsets of $\mathcal{S}_3$, each consisting of 12.5% of the $\mathcal{S}_3$ population ($\mathcal{S}_{3,1}$ and $\mathcal{S}_{3,2}$), are assigned to follow the challengers by modifying their social velocity ($\boldsymbol{v}_{i,\mathrm{s}} = \boldsymbol{x}_{\mathrm{ch}} - \boldsymbol{x}_i$). Lastly, a subset comprised of 25% of $\mathcal{S}_3$ is assigned a random velocity perturbation $\boldsymbol{v}_{\mathrm{rnd}}$ drawn from a normal distribution ($\boldsymbol{V} = \boldsymbol{V} + \boldsymbol{v}_{\mathrm{rnd}}$), while the remaining 50% of $\mathcal{S}_3$ has its velocity unchanged. This randomization helps prevent convergence to local minima.

The second population in the PSOGA algorithm follows a modified GA approach [52], with some adaptations. In each iteration, a fitness-based tournament selection method is used to choose the individuals from the current population as parents for the next generation. A member can be selected as a parent multiple times. The parents are paired up, and each pair produces two children. The children's identity (the input vector $\boldsymbol{x}$) is represented by a set of binary genes (0s and 1s), and is generated through crossover, where a certain number of genes come from one parent and the remaining genes come from the other parent. These binary genes also have a chance to undergo mutations, where 0s can turn into 1s or vice versa.

If, at any iteration, the PSO swarm has a better overall recorded position, after the creation of children, the best particle found in the PSO swarm ($\boldsymbol{x}_{\mathrm{best,PSO}}$) is combined as a parent with the best individual from the GA population ($\boldsymbol{x}_{\mathrm{best,GA}}$). Children involving these parents are generated until 10% of the current GA generation has been replaced.

If the GA population fails to improve for three consecutive iterations, 20% of the children in the current generation have their mutation probability tripled. This adjustment helps introduce additional exploration in the population and helps to escape from potential local optima.

A schematic representation of the PSOGA algorithm is shown in Fig. 6.

4.2. Cost function

To uniquely define the optimization problem, a cost function to minimize is required. The aim pursued in this paper is to maximize the payload ratio for the analyzed lunar ascent mission. For this reason, the cost function has been written as follows:

$$f(\boldsymbol{x}) = \frac{c_{\mathrm{u}}}{\lambda} + c_{\mathrm{h}}\Delta h + c_{\mathrm{v}}\Delta v + c_{\theta}\Delta\theta \tag{34}$$

where λ is the payload ratio $\lambda = \frac{m_{\mathrm{u}}}{m_0}$, Δh, Δv, $\Delta\theta$ are the constraints introduced in Section 3.3 to ensure the target orbit has been reached, and c_i is the weight of the ith term. Notice that an equatorial launch towards an equatorial orbit allows refraining from the enforcement of the inclination terminal constraint.

In order to make the optimization work as intended, the weight of each term must be carefully chosen. In particular, the weights applied to the three constraints (altitude, velocity, and direction) have been designed as follows:

$$c_i = \begin{cases} c_{i,0}, & \text{if } \Delta_i > \delta_i \\ c_{i,0} e^{c_{i,1}(\Delta_i - \delta_i)}, & \text{if } \Delta_i \leq \delta_i \end{cases} \tag{35}$$

where i represents a constrained variable, Δ_i is the displacement with respect to the objective, and δ_i is the associated tolerance, introduced in Section 3.3. This way, the optimization prioritizes the reduction of terminal errors only at the beginning. Once the constraints are met, the focus is shifted to the maximization of the payload ratio. An early trial and error process has been performed to select suitable weights that would consistently ensure the fulfillment of the constraints while returning satisfactory payload ratio values. These are:

$$\begin{aligned} c_{\mathrm{u}} &= 100 \\ c_{h,0} &= 0.01\ \mathrm{m}^{-1} \quad & c_{h,1} &= 50\ \mathrm{m}^{-1} \\ c_{v,0} &= 2\ (\mathrm{m/s})^{-1} \quad & c_{v,1} &= 0.2\ (\mathrm{m/s})^{-1} \\ c_{\theta,0} &= 500\ \mathrm{rad}^{-1} \quad & c_{\theta,1} &= 80\ \mathrm{rad}^{-1} \end{aligned} \tag{36}$$

5. Results and discussion

The integrated design of a pressure-fed HRM and of the ascent trajectory has been conducted for a single-stage launch vehicle. The objective is to optimize the HRM design, thrust direction, and flight parameters to maximize the payload ratio for a nominal mission that targets a 100 km circular lunar orbit on the equatorial plane.

A schematic representation of the entire multi-disciplinary optimization problem is shown in Fig. 7. The range of variation of the design parameters is reported in Table 3. It is recalled that the range of variation of the pre-exponential factor, a, depends on the propellant combination choice, as specified in Section 2.

A preliminary analysis is conducted to investigate the influence of the total number of particles used in the PSOGA optimization on the obtained solution. Fig. 8 demonstrates that the cost function plateaus are very close to each other beyond a certain particle count, indicating the reliability of the results. Hence, for the current problem, a total population of 10,000 particles is employed.

The optimized design and flight parameters obtained from the optimization process are summarized in Table 4 for both LOX/Wax

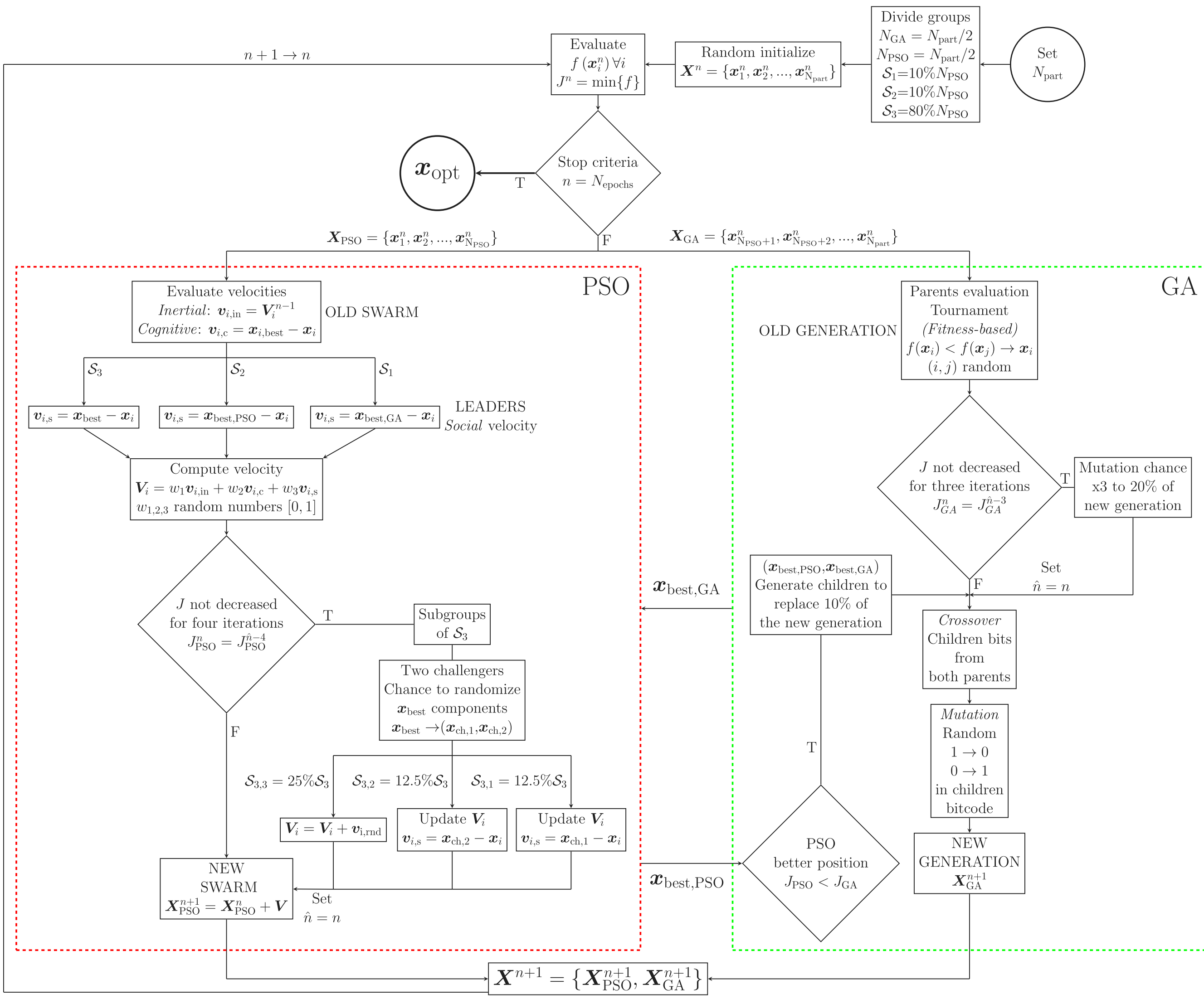

Fig. 6. Flowchart of the PSOGA algorithm.

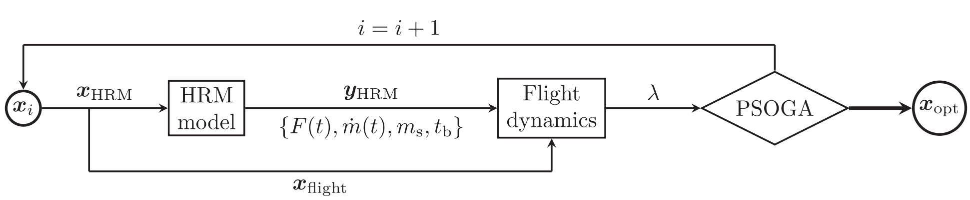

Fig. 7. Flowchart of the integrated optimization procedure.

Table 3
Design parameters domain.

$\boldsymbol{x}_{\rm HRM}$	L_g [m]	$D_{p,0}$ [m]	$D_{t,0}$ [m]	ε_0 [–]	$\dot{m}_{ox,0}$ [kg/s]	$\dot{m}_{ox,2}$ [kg/s]	a [mm/s · (m^{2}s/kg)^n]	t_b [s]
	$[0.1, 2]$	$[0.1, 0.4]$	$[0.05, 0.3]$	$[10, 100]$	$[0.5, 5]$	$[0.2, 3]$	$[0.13, 0.3]$ – $[0.016, 0.09]$	$[100, 500]$
$\boldsymbol{x}_{\rm flight}$	h_{LO} [m]	θ_{PO} [deg]	t_{PO} [s]	$\theta_{blt,f}$ [deg]	ξ [–]	t_1 [s]	t_{co} [s]	θ_{orb} [deg]
	$[75, 350]$	$[0, 90]$	$[5, 50]$	$[-45, 45]$	$[-1, 0]$	$[100, 400]$	$[0, 4000]$	$[-15, 15]$

and H_2O_2(90%)/HDPE configurations. It is noteworthy that the optimized value of the design parameter t_{PO} is located at the boundary of its defined range. While this suggests that a further improvement could be achieved by expanding the parameter range, it is important to acknowledge the technical and practical constraints. Specifically, performing a programmed nozzle rotation within a time frame smaller than 5 s is deemed unrealistic. As for the stand-off distance between the LV and the launch pad, h_{LO}, which is also at the lower limit of its

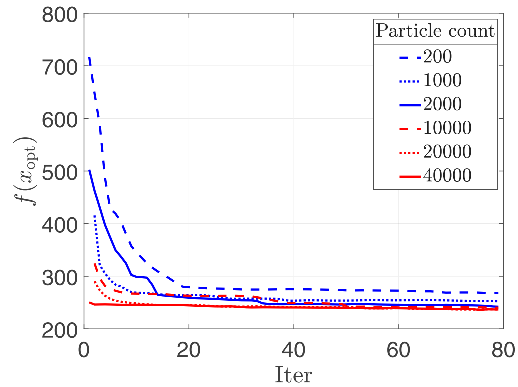

Fig. 8. PSOGA sensitivity analysis.

Table 4
Optimum solution vector.

x_{flight}	LOX/Wax	H_2O_2/HDPE	x_{HRM}	LOX/Wax	H_2O_2/HDPE
h_{LO} [m]	75	75	L_g [m]	0.963	0.945
θ_{PO} [deg]	18.2	29.3	$D_{\mathrm{p,0}}$ [m]	0.194	0.191
t_{PO} [s]	5	5	$D_{\mathrm{t,0}}$ [m]	0.096	0.082
$\theta_{\mathrm{blt},f}$ [deg]	3.63	4.68	ϵ_0 [–]	29.0	22.3
ξ [–]	−0.36	−0.40	$\dot{m}_{\mathrm{ox,0}}$ [kg/s]	1.400	1.458
t_1 [s]	207	273	$\dot{m}_{\mathrm{ox,2}}$ [kg/s]	0.416	0.478
t_{co} [s]	2989	3296	a [mm/s $\cdot$ (m^{2}s/kg)^n]	0.150	0.072
θ_{orb} [deg]	−0.32	−0.31	t_b [s]	211	278

Table 5
Initial (v_i) and final (v_f) inertial velocity, velocity losses, and rocket Δv_{prop}.

	v_i [m/s]	v_f [m/s]	Δv_{grav} [m/s]	Δv_{mis} [m/s]	Δv_{prop} [m/s]
LOX/Wax	4.6	1625	−134.2	−17.6	1772.2
H_2O_2/HDPE			−146.0	−18.4	1784.8

defined range, further reductions are not feasible as it would violate the minimum stand-off distance required during lift-off. The obtained value represents the practical lower limit that ensures safe launch conditions. These parameters (t_{PO} and h_{LO}) are the only ones at the boundaries of their domain, ensuring that the solution is actually a global optimum.

Table 5 reports the initial and final inertial velocity of the vehicle, v_i and v_f, the cumulative amount of gravitational (Δv_{grav}), and misalignment (Δv_{mis}) losses, and the velocity increment provided by the propulsion system, Δv_{prop}, along the ascent trajectory. It is noteworthy that, due to the Moon small gravitational pull, the ideal $\Delta v = v_f - v_i$ is almost equal to the propulsive Δv_{prop}.

The mass distribution among the different subsystems (respectively oxidizer, fuel, combustion chamber, oxidizer tank, nozzle, feeding system, contingencies, catalytic bed, shrouds, and ancillaries) and the HRM dimensions are summarized in Table 6, with k_s being the rocket structural coefficient, defined as $k_s = \dfrac{m_s}{m_p + m_s}$.

A summary of the operating conditions of the optimal hybrid rockets design, averaged over the total burning time (considering both burns), is shown in Table 7. These operating conditions are a direct result of the mission requirements for lunar ascent. Unlike launch vehicles operating on Earth, a lunar ascent trajectory does not have the atmospheric drag and experiences lower gravitational forces. Consequently, the optimal design favors lower thrust and chamber pressure to save structural mass. This leads to an average thrust of approximately 5.20 or 6.70 kN (depending on the propellant combination) and to a chamber pressure of about 5 bar. The optimizer prioritizes improving the structural coefficient of the hybrid rocket by reducing dimensions and material thickness rather than compensating for gravitational losses with higher thrust or rather than increasing specific impulse through higher chamber pressure. It is noteworthy that the pre-exponential factor, a, for LOX/Wax approaches the lower limit of its design space, while for H_2O_2(90%)/HDPE it tends towards the upper limit. This suggests that achieving an optimal configuration requires less swirl for LOX. This could be attributed to wax liquefying nature, which leads to inherently higher fuel regression rates, whereas HDPE low regression rate necessitates swirl injection to attain sufficient thrust. The average mixture ratio, approximately 1.9 for LOX/Wax and 5.2 for H_2O_2(90%)/HDPE, is selected to be around the optimal value, leading to an average specific impulse of, respectively, 312.8 and 300.0 s. Note that the average O/F is slightly lower than the one associated to maximum theoretical performance, as the optimizer favors slightly fuel-rich conditions to mitigate throat erosion. The operating conditions of the optimized configurations are similar to the operating conditions of other optimized HRMs for extraterrestrial ascent missions, such as the Mars ascent missions described in [53,54]. It is important to underline that the optimal configurations satisfy the 5 g axial acceleration constraint, with the maximum a_x during the trajectory being 1.15 g for LOX/Wax and 0.91 g for H_2O_2(90%)/HDPE. Note that none of the values reported in Table 7 seem to raise concerns for practical applications since operational parameters are neither too large or too small with respect to the state of the art. Similar values of regression rate and O/F can be found in [55] for H_2O_2/HDPE, and in [24] for GOX/Wax, which also shows a similar chamber pressure with respect to the optimized launch vehicle. Comparable O/F for GOX/Wax can be found in [26]. A similar oxidizer mass flow rate is used in [39], for a H_2O_2/HTPB propellant combination aimed at testing the performance of catalytic beds. Lastly, a similar thrust can be found in [56] (6 kN), in a HRE concept design of a Mars Ascent Vehicle developed and tested at JPL.

A single-stage hybrid rocket is therefore capable of successfully carrying out the proposed lunar ascent mission, using two separate burns and a coasting phase to minimize the energy requirement. With respect to a two-stage configuration (needed for example when using solid rockets), a single-stage is less complex and less expensive. In addition, the need to recover only one stage improves the reusability of the launch vehicle.

When comparing propellant combinations, the average specific impulse of LOX is higher than that of hydrogen peroxide by approximately

Table 6
Optimal HRMs mass budget and dimensions.

	m_{ox} [kg]	m_{fu} [kg]	m_c [kg]	m_{tk} [kg]	m_{noz} [kg]	m_{feed} [kg]	m_{cont} [kg]	m_{bed} [kg]	m_{sh} [kg]	m_{anc} [kg]	L_{tot} [m]	D_{tot} [m]	k_s [–]
LOX	300.4	157.9	18.34	5.85	32.15	7.45	13.75	–	1.90	8.83	3.604	0.526	0.161
H_2O_2	408.6	78.56	9.90	4.89	31.33	7.69	14.62	7.02	1.44	8.54	5.019	0.386	0.149

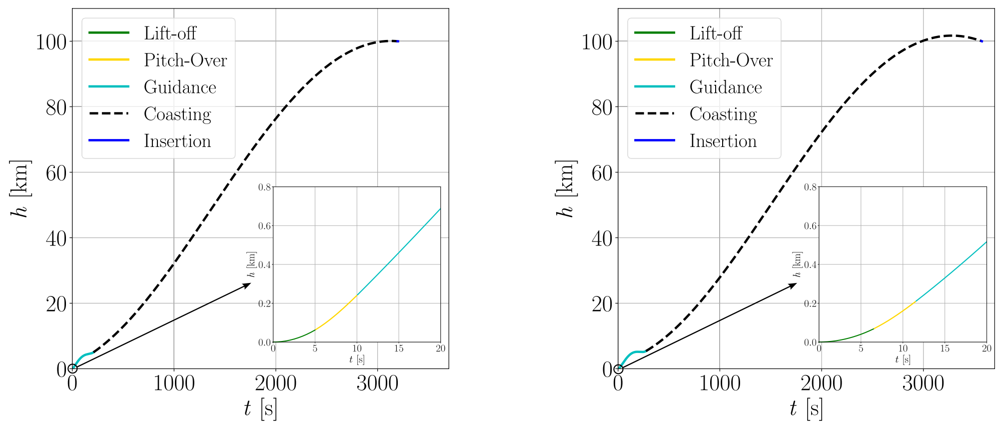

(a) LOX/Wax. (b) H_2O_2(90%)/HDPE.

Fig. 9. Launch vehicle altitude time–history.

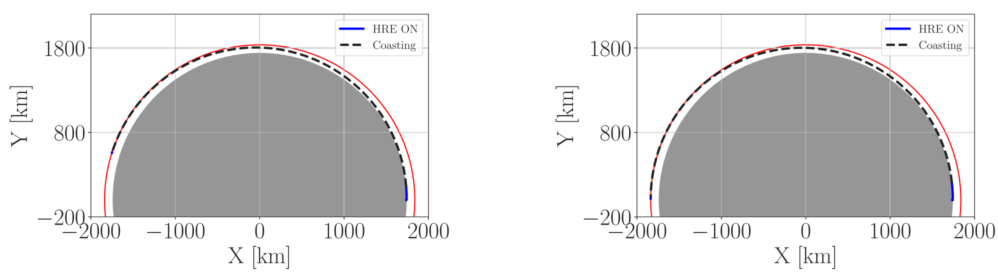

(a) LOX/Wax. (b) H_2O_2(90%)/HDPE.

Fig. 10. Launch vehicle 2-D trajectory (Moon equatorial plane).

Table 7
Optimal HRMs operating conditions, averaged over time, and LV initial and final mass.

	F_{max} [kN]	O/F [–]	p_c [bar]	$\dot{r}$ [mm/s]	I_{sp} [s]	I_{tot} [kNs]	m_0 [kg]	m_f [kg]	λ [–]
LOX/Wax	6.88	1.90	4.83	0.780	312.8	1412	1047	588	0.4777
H_2O_2/HDPE	5.26	5.18	4.91	0.346	300.0	1438	1073	585	0.4662

13 s (4.3%). H_2O_2(90%)/HDPE, instead, presents a structural coefficient about 1.2% lower than the LOX/Wax combination because of the mass savings associated with the lighter tank and combustion chamber, owing to the use of more volumetrically efficient propellants. The LOX/Wax propellant combination provides a 1.15% higher payload ratio compared to the H_2O_2(90%)/HDPE combination, equivalent to a weight reduction of approximately 26 kg in the LV lift-off mass. This improvement is attributed to the higher I_{sp} of LOX, leading to a lower propellant consumption, and to the increased thrust achievable by liquefying fuels, leading to a reduction in gravitational losses (approximately 8.1% lower for LOX/Wax compared to the hydrogen peroxide combination).

Figs. 9 and 10 illustrate the optimized trajectory of the launch vehicles for both propellant combinations. In particular, Fig. 9 depicts the altitude-time profile of the optimized flight path, while Fig. 10 presents the trajectory projected onto the 2-D equatorial plane of the Moon. The launch vehicle initially follows a direct ascent until an altitude of 6 km has been reached. At this point, with the flight path angle near zero, the altitude remains in close proximity to this value while the velocity continues to increase until the end of the first HRM burn. The attained velocity enables the vehicle to enter a Hohmann-like transfer orbit. A prolonged coasting phase, lasting approximately half of an orbital period, is performed until reaching the target altitude. Subsequently, a brief second ignition of the HRM is conducted to adjust the final velocity direction and to increase the transfer orbit energy to match that of the desired circular orbit. The utilization of a Hohmann-like transfer represents the optimal mission scenario for injecting the launch vehicle into the target orbit and is made possible by the restart capabilities of the propulsion system employed. It is evident that the two propellant combinations exhibit minimal differences in their mission profiles. With the exception of a small difference in the coasting time and a slightly different shape of the transfer orbit, the trajectories of the LVs are very similar. This similarity arises because the optimal trajectory must be as close as possible to an Hohmann transfer, independently of the specific propellant combination employed.

Figs. 11 and 12 present the thrust elevation (defined in Section 3.1, Fig. 4) and the flight path angle during the BLT guidance (Fig. 11) and orbit insertion (Fig. 12) phases. During the initial HRM firing (Fig. 11), the BLT guidance strategy effectively adjusts the launch vehicle attitude to achieve a gradual tilt, facilitating rapid altitude gain and minimizing gravitational losses. Simultaneously, it maintains a relatively small misalignment between the thrust direction and inertial velocity, and achieves a small final flight-path angle. This approach aims to minimize misalignment losses and aims to prepare the vehicle

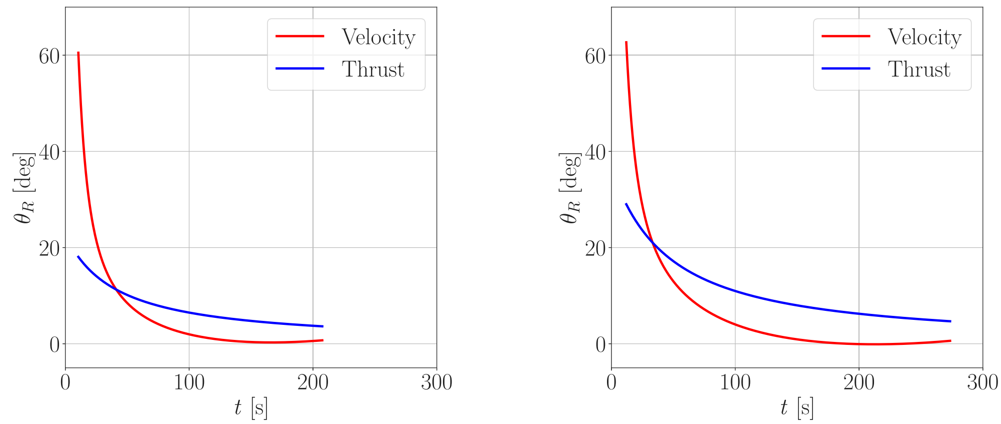

(a) LOX/Wax. (b) H_2O_2(90%)/HDPE.

Fig. 11. Thrust elevation and flight-path angle during guidance.

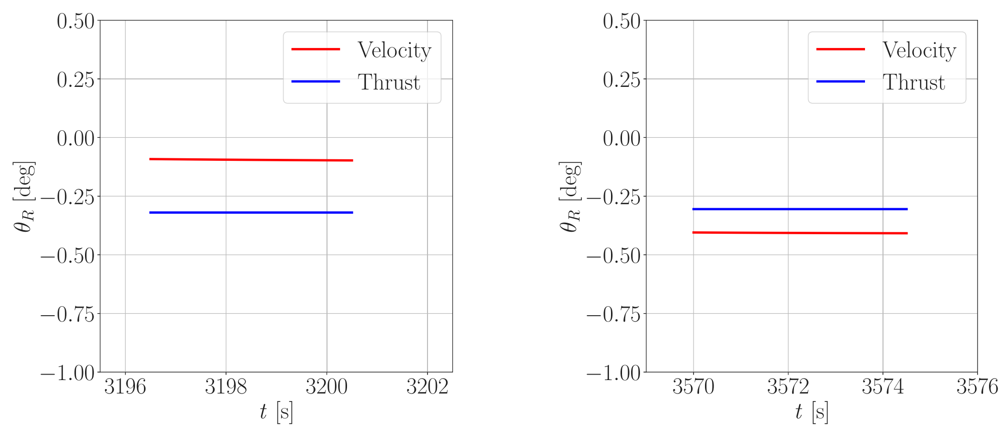

(a) LOX/Wax. (b) H_2O_2(90%)/HDPE.

Fig. 12. Thrust elevation and flight-path angle during orbit insertion.

for the subsequent phase of orbit insertion. It is interesting to note the high angular difference between thrust and velocity at the beginning of the BLT guidance, respectively 40 degrees for LOX and 30 degrees for H_2O_2. This result stems from the optimizer attempt to tilt the LV horizontally as fast as possible in order to reduce gravitational losses. This fast tilting is possible in such a mission scenario as there is no Qα constraint nor drag force. It is clear that such high TVC actuation angles might prove technologically challenging to achieve. However, TVC technical constraints are not considered at this stage as they are not well known in the literature for the mission scenario under consideration. Nevertheless, such a constraint could be easily implemented by slightly reducing the kick angle, θ_{PO}, at the end of the pitch-over and by slightly increasing the pitch-over duration, t_{PO}, without affecting the quality of the results.

In the second HRM firing (Fig. 12), instead, the thrust elevation is close to zero, as expected during a well-performed Hohmann-like transfer. For the same reasons as for the trajectory, guidance of the LVs is very similar between the two propellant combinations.

Despite the similar mission profiles, differences between the chosen propellant combinations can be seen when considering the LVs operating conditions. Fig. 13 displays the time-dependent profiles of vacuum thrust and mass flow rate for the HRMs, Fig. 14 depicts the chamber pressure and throat diameter, and Fig. 15 shows the characteristic velocity and mixture ratio (excluding the coasting phase). The observed behavior of each parameter aligns with typical expectations for pressure-fed hybrid rocket systems with the chosen propellant combinations. When LOX/Wax is considered, the slight decrease in thrust and mass flow rate is a direct consequence of grain regression, as $\dot{m}_{fu} \propto D_p^{1-2n}$ (rearranging Eqs. (3) and (4)). The decrease in chamber pressure, instead, is mainly an effect of throat erosion, as $p_c = \dot{m}_e c^* / A_t$ (rearranging Eq. (5)). The increase in mixture ratio throughout the burn is typical of propellants with a mass flux coefficient $n > 0.5$ (Eq. (22)). As for H_2O_2(90%)/HDPE, the observed decrease in chamber pressure can still be attributed to throat erosion. However, thrust and mass flow rate show a slight increase over time. This behavior can be attributed to the use of a pressure-fed system and to the value of the mass flux coefficient, n. In fact, the oxidizer mass flow rate increases over time due to the reduction in chamber pressure ($\dot{m}_{ox} \propto p_{tk} - p_h$, Eq. (2)). Mass flow rate decay associated with grain regression is instead not present due to the mass flux coefficient $n = 0.5$ ($\dot{m}_{fu} \propto D_p^{1-2n}$). Consequently, the mixture ratio exhibits a monotonically increasing trend, which is also in line with Eq. (22).

An in scale 2-D view of the two HRM configurations is shown in Fig. 16. It is evident that the primary distinction between the two configurations pertains to the oxidizer tank length and the stage diameter. In the case of hydrogen peroxide, owing to the considerably higher operating mixture ratio, the oxidizer tank is significantly larger, nearly doubling the size of the LOX configuration tank. Conversely, the diameter of the hydrogen peroxide rocket is smaller due to the utilization of a pyrolyzing fuel, resulting in a reduced grain regression rate. Consequently, to attain the required thrust, a longer grain becomes necessary, and despite the smaller fuel mass, the chamber length of the hydrogen peroxide configuration remains essentially the same of the LOX one.

Overall, the LOX configuration offers a slightly better payload ratio. However, the restarting capabilities and the easier storability of the

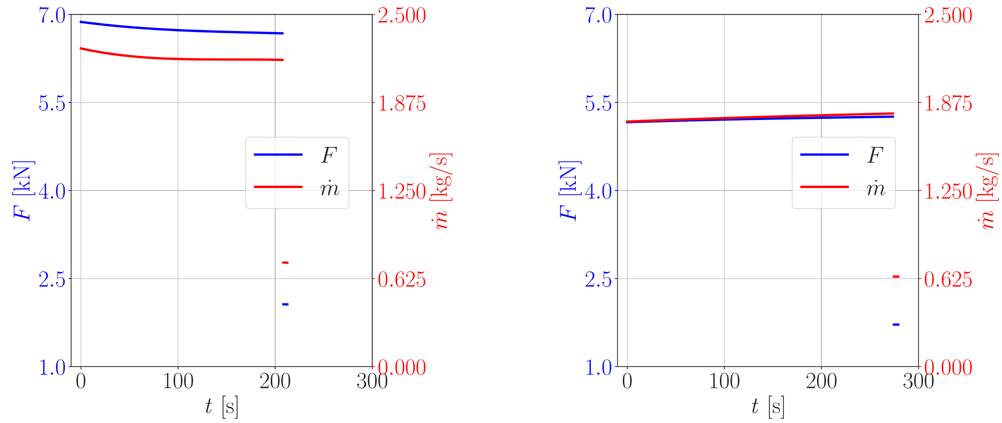

(a) LOX/Wax. (b) H_2O_2(90%)/HDPE.

Fig. 13. Thrust and mass flow rate time–history (without coasting).

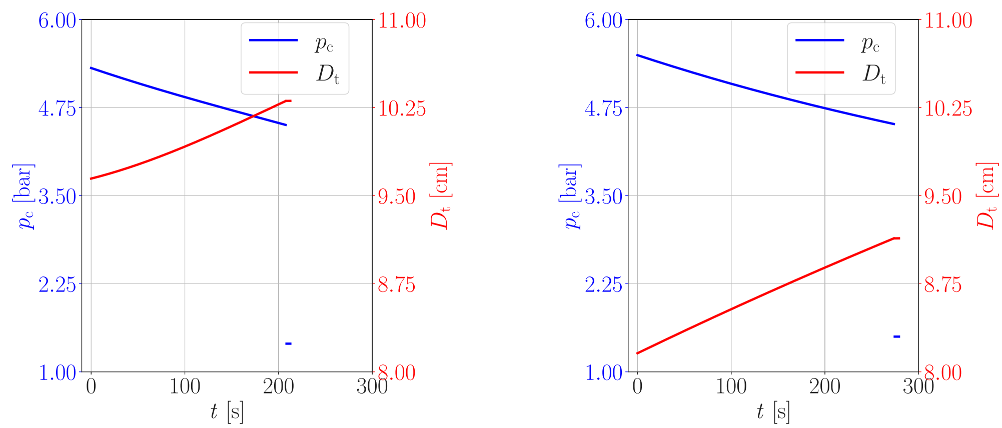

(a) LOX/Wax. (b) H_2O_2(90%)/HDPE.

Fig. 14. Chamber pressure and throat diameter time–history (without coasting).

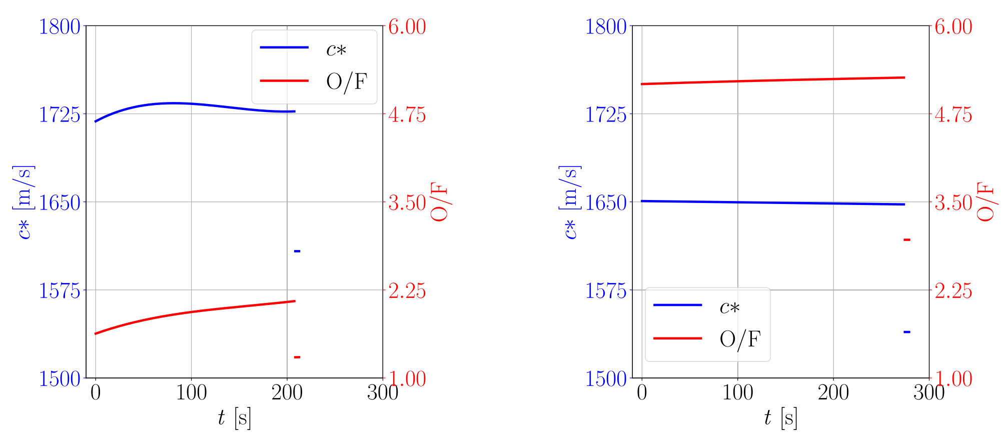

(a) LOX/Wax. (b) H_2O_2(90%)/HDPE.

Fig. 15. Characteristic velocity and mixture ratio time–history (without coasting).

hydrogen peroxide combination, along with the improved mechanical properties of HDPE with respect to pure paraffin-wax, might be key factors in the propellant selection process.

The HRM configuration that utilizes hydrogen peroxide 90% and high-density polyethylene as propellants features a propellant mass $m_{prop} = 487.16\,\mathrm{kg}$ and a dry mass $m_s = 85.43\,\mathrm{kg}$. The rocket is 5.019 m long and 0.386 m wide ($L/D = 13.00$). The total burning time t_b is divided into two phases t_1 (ascent trajectory) and t_2 (orbit insertion), respectively 273 s and 5 s. A maximum payload ratio $\lambda = 0.4662$ ($m_u = 500$ kg and $m_0 = 1073$ kg) is injected into the target orbit. This is consistent with a propulsive $\Delta v = 1784.8$ m/s (see Table 5), $k_s = 0.149$ (see Table 6), and $I_{sp} = 300.0$ s (see Table 7), according to Tsiolkovsky's equation.

6. Conclusions

This paper proposes the use of a single-stage hybrid rocket with swirl injection for a lunar ascent mission, targeting a 100 km circular

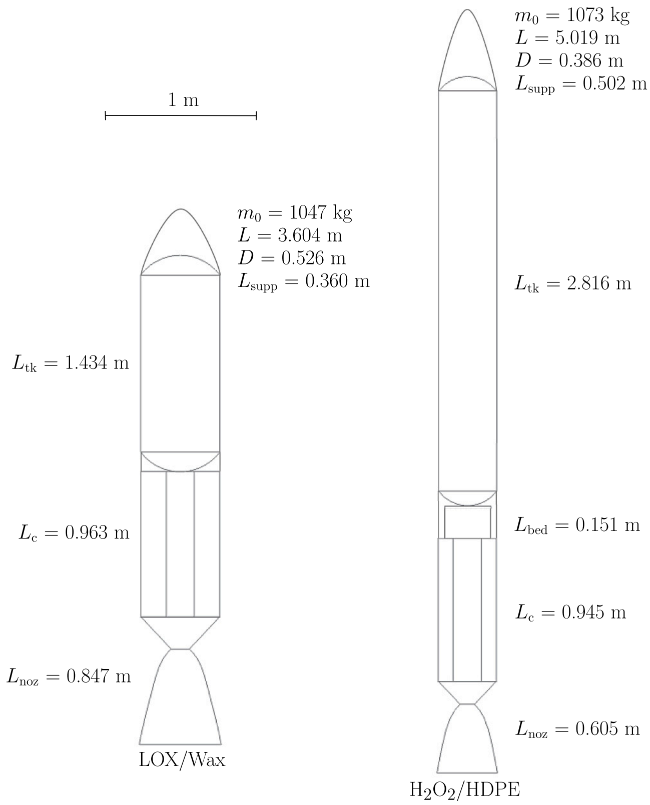

Fig. 16. 2-D view of the optimal HRM configurations, in scale.

orbit on the equatorial plane. To this aim, a multi-disciplinary optimization problem has been formulated, where the HRM design and ascent trajectory are concurrently optimized. The goal is to maximize the payload ratio carried into the target orbit while meeting a number of constraints related to the motor dimensions and to the payload structural integrity.

In this context, a 0-D internal ballistics model is used to evaluate the performance and gross mass of a specific HRM design, defined by a set of parameters that identify its geometrical dimensions and operating conditions. The model outputs, including thrust, mass flow rate, and gross mass, are then processed by a three-degree of freedom point-mass dynamical model, incorporating design variables for thrust direction to define the ascent trajectory.

An in-house population-based heuristic algorithm is utilized to solve the integrated optimization problem. This algorithm combines two distinct populations, each employing a different optimization approach: particle swarm optimization (PSO) and genetic algorithms (GA). The two populations interact and exchange information to find the optimal solution for the problem at hand. A preliminary analysis verifies the insensitivity of the solution to the algorithm population size.

The obtained results demonstrate the feasibility of the proposed propulsion system for the investigated lunar ascent mission. The single-stage configuration offers advantages such as reduced complexity, lower cost, and enhanced reusability compared to a two-stage setup. The utilization of hybrid rocket propulsion restart capabilities enables the efficient implementation of a coasting phase between the direct ascent and orbit insertion, resulting in a highly effective Hohmann-like transfer.

Two propellant combinations are considered: LOX/Wax and H_2O_2(90%)/HDPE. In the case of LOX/Wax, the high-performance characteristics of liquid oxygen are acknowledged, but challenges related to its cryogenic nature and handling complexities are also taken into account. Additionally, the need for dual igniters to achieve restart capabilities introduces uncertainties regarding the second ignition. Conversely, the H_2O_2(90%)/HDPE combination presents several advantages. Hydrogen peroxide as a storable propellant eliminates the difficulties associated with cryogenic handling. Moreover, the decomposed oxidizer from the catalytic bed acts as a hypergolic propellant with HDPE, circumventing the ignition challenges encountered with LOX/Wax. Lastly, the use of HDPE offers more reliable grain mechanical properties with respect to pure paraffin-wax. Despite the payload ratio associated to the LOX configuration is 1.15% higher than the one associated to hydrogen peroxide, resulting in a weight reduction of about 26 kg, overall, based on a comprehensive evaluation of feasibility and performance considerations, the analysis concludes that the H_2O_2(90%)/HDPE combination emerges as the preferred propellant choice for the proposed lunar ascent mission.

Future work involves the analysis of lunar ascent missions to higher lunar orbits, such as missions to the Lunar Orbital Platform-Gateway which should be placed in HALO orbit with a perilunar altitude of approximately 1630 km [10]. In addition, in-situ resources might be considered as propellants or launch vehicle materials in order to assess their effects on performance.

CRediT authorship contribution statement

Paolo Maria Zolla: Writing – original draft, Visualization, Software, Methodology, Formal analysis. **Rodrigo Rosa:** Validation, Software, Investigation, Data curation. **Mario Tindaro Migliorino:** Writing – review & editing, Supervision, Conceptualization. **Daniele Bianchi:** Writing – review & editing, Supervision, Project administration, Conceptualization.

Declaration of competing interest

The authors declare that they have no known competing financial interests or personal relationships that could have appeared to influence the work reported in this paper.

References

[1] H. Zhu, H. Tian, G. Cai, W. Bao, Uncertainty analysis and design optimization of hybrid rocket motor powered vehicle for suborbital flight, Chin. J. Aeronaut. 28 (3) (2015) 676–686, http://dx.doi.org/10.1016/j.cja.2015.04.015.

[2] A. Okninski, On use of hybrid rocket propulsion for suborbital vehicles, Acta Astronaut. 145 (2018) 1–10, http://dx.doi.org/10.1016/j.actaastro.2018.01.027.

[3] L. Casalino, F. Masseni, D. Pastrone, Uncertainty analysis and robust design for a hybrid rocket upper stage, J. Spacecr. Rockets 56 (5) (2019) 1424–1431, http://dx.doi.org/10.2514/1.A34422.

[4] L. Casalino, F. Masseni, D. Pastrone, Robust design approaches for hybrid rocket upper stage, J. Aerosp. Eng. 32 (6) (2019) http://dx.doi.org/10.1061/(ASCE)AS.1943-5525.0001078.

[5] E.T. Jens, B.J. Cantwell, G.S. Hubbard, Hybrid rocket propulsion systems for outer planet exploration missions, Acta Astronaut. 128 (2016) 119–130, http://dx.doi.org/10.1016/j.actaastro.2016.06.036.

[6] O. Kara, H. Karakaş, M.A. Karabeyoğlu, Hybrid rockets with mixed N2O/CO2 oxidizers for mars ascent vehicles, Acta Astronaut. 175 (2020) 254–267, http://dx.doi.org/10.1016/j.actaastro.2020.05.060.

[7] A.A. Chandler, B.J. Cantwell, G. Scott Hubbard, A. Karabeyoglu, Feasibility of a single port hybrid propulsion system for a Mars ascent vehicle, Acta Astronaut. 69 (11) (2011) 1066–1072, http://dx.doi.org/10.1016/j.actaastro.2011.07.004.

[8] D.R. Sparks, Hybrid rocket propellants from lunar material, Acta Astronaut. 17 (10) (1988) 1093–1097, http://dx.doi.org/10.1016/0094-5765(88)90192-0.

[9] E. Stoll, P. Härke, S. Linke, F. Heeg, S. May, The regolith rocket–A hybrid rocket using lunar resources, Acta Astronaut. 179 (2021) 509–518, http://dx.doi.org/10.1016/j.actaastro.2020.11.022.

[10] T. Gill, NASA's lunar orbital platform-gateway, in: 45th Space Congress, Cape Canaveral, Feb. 2018.

[11] L. Casalino, D. Pastrone, F. Simeoni, Hybrid rocket upper stage optimization: Effects of grain geometry, in: 47th AIAA/ASME/SAE/ASEE Joint Propulsion Conference & Exhibit, San Diego, CA, USA, 2011, http://dx.doi.org/10.2514/6.2011-6024.

[12] L. Casalino, F. Letizia, D. Pastrone, Optimization of hybrid upper-stage motor with coupled evolutionary/indirect procedure, J. Propuls. Power 30 (5) (2014) 1390–1398, http://dx.doi.org/10.2514/1.B35111.

[13] L. Casalino, F. Masseni, D. Pastrone, Deterministic and robust optimization of hybrid rocket engines for small satellite launchers, J. Spacecr. Rockets 58 (6) (2021) 1893–1903, http://dx.doi.org/10.2514/1.A35007.

[14] A. Zavoli, P.M. Zolla, L. Federici, M.T. Migliorino, D. Bianchi, Machine learning techniques for flight performance prediction of hybrid rocket engines, in: AIAA Propulsion and Energy Forum, Virtual event, 2021, http://dx.doi.org/10.2514/6.2021-3506.

[15] A. Zavoli, P. Maria Zolla, L. Federici, M.T. Migliorino, D. Bianchi, Surrogate neural network for rapid flight performance evaluation of hybrid rocket engines, J. Spacecr. Rockets 59 (6) (2022) 2003–2016, http://dx.doi.org/10.2514/1.A35369.

[16] G. Cai, H. Zhu, D. Rao, H. Tian, Optimal design of hybrid rocket motor powered vehicle for suborbital flight, Aerosp. Sci. Technol. 25 (1) (2013) 114–124, http://dx.doi.org/10.1016/j.ast.2011.12.014.

[17] W. Pengcheng, T. Hui, Z. Hao, C. Guobiao, Multi-disciplinary design optimization with fuzzy uncertainties and its application in hybrid rocket motor powered launch vehicle, Chin. J. Aeronaut. 33 (5) (2020) 1454–1467, http://dx.doi.org/10.1016/j.cja.2019.11.002.

[18] P. Zolla, R. Rosa, M.T. Migliorino, D. Bianchi, Multi-disciplinary optimization of single-stage hybrid rocket with swirl injection for lunar ascent, in: AIAA SciTech Forum, National Harbor, MD, USA, 2023, http://dx.doi.org/10.2514/6.2023-2349.

[19] P.M. Zolla, M.T. Migliorino, D. Bianchi, F. Nasuti, R.C. Pellegrini, E. Cavallini, A computational tool for the design of hybrid rockets, Aerotecnica Missili Spazio 100 (3) (2021) 253–262, http://dx.doi.org/10.1007/s42496-021-00085-3.

[20] G. Leccese, E. Cavallini, M. Pizzarelli, State of art and current challenges of the paraffin-based hybrid rocket technology, in: AIAA Propulsion and Energy Forum, Indianapolis, IN, USA, 2019, http://dx.doi.org/10.2514/6.2019-4010.

[21] L. Casalino, F. Masseni, D. Pastrone, Viability of an electrically driven pump-fed hybrid rocket for small launcher upper stages, Aerospace 6 (3) (2019) http://dx.doi.org/10.3390/aerospace6030036.

[22] F.D.A. Quadros, P.T. Lacava, Swirl injection of gaseous oxygen in a lab-scale paraffin hybrid rocket motor, J. Propuls. Power 35 (5) (2019) 896–905, http://dx.doi.org/10.2514/1.B37283.

[23] T. Takashi, S. Yuasa, K. Yamamoto, Effects of swirling oxidizer flow on fuel regression rate of hybrid rockets, in: 35th Joint Propulsion Conference and Exhibit, Los Angeles, CA, USA, 1999, http://dx.doi.org/10.2514/6.1999-2323.

[24] M.T. Migliorino, M. Fabiani, C. Paravan, D. Bianchi, F. Nasuti, L. Galfetti, R.C. Pellegrini, E. Cavallini, Numerical and experimental analysis of fuel regression rate in a lab-scale hybrid rocket engine with swirl injection, Aerosp. Sci. Technol. 140 (2023) 108467, http://dx.doi.org/10.1016/j.ast.2023.108467.

[25] M. Franco, F. Barato, E. Paccagnella, M. Santi, A. Battiston, A. Comazzetto, D. Pavarin, Regression rate design tailoring through vortex injection in hybrid rocket motors, J. Spacecr. Rockets 57 (2) (2020) 278–290, http://dx.doi.org/10.2514/1.A34539.

[26] M.A. Karabeyoglu, G. Zilliac, B.J. Cantwell, S. DeZilwa, P. Castellucci, Scale-up tests of high regression rate paraffin-based hybrid rocket fuels, J. Propuls. Power 20 (6) (2004) 1037–1045, http://dx.doi.org/10.2514/1.3340.

[27] E. Toson, A.M. Karabeyoglu, Design and optimization of hybrid propulsion systems for in-space application, in: 51st AIAA/SAE/ASEE Joint Propulsion Conference, Orlando, FL, USA, 2015, http://dx.doi.org/10.2514/6.2015-3937.

[28] E. Paccagnella, M. Santi, A. Ruffin, F. Barato, D. Pavarin, G.A. Misté, G. Venturelli, N. Bellomo, Testing of a long-burning-time paraffin-based hybrid rocket motor, J. Propuls. Power 35 (2) (2019) 432–442, http://dx.doi.org/10.2514/1.B37144.

[29] E.J. Wernimont, S.D. Heister, Combustion experiments in hydrogen peroxide/polyethylene hybrid rocket with catalytic ignition, J. Propuls. Power 16 (2) (2000) 318–326, http://dx.doi.org/10.2514/2.5571.

[30] S. Kang, D. Lee, E. Lee, S. Kwon, Design and performance evaluation of hybrid rocket using 95 wt.% H2O2, in: 52nd AIAA/SAE/ASEE Joint Propulsion Conference, Salt Lake City, UT, USA, 2016, http://dx.doi.org/10.2514/6.2016-4864.

[31] S. Gordon, B.J. McBride, Computer Program for Calculation of Complex Chemical Equilibrium Compositions and Applications, Tech. Rep. NASA-RP-1311, NASA, 1996, URL https://ntrs.nasa.gov/citations/19950013764.

[32] D. Bianchi, M.T. Migliorino, M. Rotondi, L. Kamps, H. Nagata, Numerical analysis of nozzle erosion in hybrid rockets and comparison with experiments, J. Propuls. Power 38 (3) (2022) 389–409, http://dx.doi.org/10.2514/1.B38547.

[33] D. Bianchi, F. Nasuti, Numerical analysis of nozzle material thermochemical erosion in hybrid rocket engines, J. Propuls. Power 29 (3) (2013) 547–558, http://dx.doi.org/10.2514/1.B34813.

[34] M.T. Migliorino, D. Bianchi, F. Nasuti, Graphite nozzle erosion trends in paraffin/oxygen hybrid rockets, J. Propuls. Power 38 (4) (2022) 508–522, http://dx.doi.org/10.2514/1.B38574.

[35] W.J. Larson, G.N. Henry, R.W. Humble, Space Propulsion Analysis and Design, McGraw-Hill, New York City, NY, USA, 1995, URL https://spacetechnologyseries.com/books/Space-Propulsion-Analysis-and-Design.html.

[36] C.P. Frank, O.J. Pinon-Fischer, D.N. Mavris, C.M. Tyl, Design methodology for the performance, weight, and economic assessment of chemical rocket engines, J. Aerosp. Eng. 30 (1) (2017) http://dx.doi.org/10.1061/(ASCE)AS.1943-5525.0000668.

[37] C. Glatt, WAATS: A Computer Program for Weights Analysis of Advanced Transportation Systems, Tech. Rep. NASA-CR-2420, NASA, 1974, URL https://ntrs.nasa.gov/citations/19740027176.

[38] S. Jung, S. Choi, S. Heo, S. Kwon, Scaling of catalyst bed for hydrogen peroxide monopropellant thrusters using catalytic decomposition modeling, Acta Astronaut. 187 (2021) 167–180, http://dx.doi.org/10.1016/j.actaastro.2021.06.027.

[39] O. Božić, D. Porrmann, D. Lancelle, S. May, Enhanced development of a catalyst chamber for the decomposition of up to 1.0 kg/s hydrogen peroxide, CEAS Space J. 8 (2) (2016) 77–88, http://dx.doi.org/10.1007/s12567-015-0109-x.

[40] Aluminium / aluminum 6061 alloy (UNS A96061), 2023, URL https://www.azom.com/article.aspx?ArticleID=6650. (Web page, Accessed: 2023).

[41] Mechanical properties of carbon fibre composite materials, fibre / epoxy resin, 2023, http://www.performance-composites.com/carbonfibre/mechanicalproperties_2.asp. (Web page, Accessed: 2023).

[42] ASM material data sheet, 2023, https://asm.matweb.com/search/SpecificMaterial.asp?bassnum=NINC34. (Web page, Accessed: 2023).

[43] F. Bennet, Lunar descent and ascent trajectories, in: 8th Aerospace Sciences Meeting, West Germany, 1970, http://dx.doi.org/10.2514/6.1970-25.

[44] R. Sostaric, Lunar Ascent and Rendezvous Trajectory Design, Tech. Rep. AAS 08-066, NASA, 2013, URL https://ntrs.nasa.gov/citations/20080009584.

[45] A.W. Markl, An Initial Guess Generator for Launch and Reentry Vehicle Trajectory Optimization (Ph.D. thesis), Ph. D., Institut für Flugmechanik und Flugregelung der Universität Stuttgart, 2001, URL https://elib.uni-stuttgart.de/bitstream/11682/3672/1/Markl_Al.pdf.

[46] F.-S. Wang, L.H. Chen, Heuristic optimization, in: Encyclopedia of Systems Biology, Springer New York, 2013, http://dx.doi.org/10.1007/978-1-4419-9863-7_411.

[47] M. Ghosh, R. Guha, I. Alam, P. Lohariwal, D. Jalan, R. Sarkar, Binary genetic swarm optimization: A combination of GA and PSO for feature selection, J. Intell. Syst. 29 (1) (2020) 1598–1610, http://dx.doi.org/10.1515/jisys-2019-0062.

[48] B. Yang, Y. Chen, Z. Zhao, A hybrid evolutionary algorithm by combination of PSO and GA for unconstrained and constrained optimization problems, in: IEEE International Conference on Control and Automation, Guangzhou, China, 2007, http://dx.doi.org/10.1109/ICCA.2007.4376340.

[49] X. Yu, A. Asma, F.M. Romany, S. Shoubao, A hybrid algorithm based on PSO and GA for feature selection, J. Cyber Secur. 3 (2) (2021) 117–124, http://dx.doi.org/10.32604/jcs.2021.017018.

[50] J. Kennedy, R. Eberhart, Particle swarm optimization, in: International Conference on Neural Networks, Perth, WA, Australia, 1995, http://dx.doi.org/10.1109/ICNN.1995.488968.

[51] W.-N. Chen, J. Zhang, Y. Lin, N. Chen, Z.-H. Zhan, H.S.-H. Chung, Y. Li, Y.-H. Shi, Particle swarm optimization with an aging leader and challengers, IEEE Trans. Evol. Comput. 17 (2) (2013) 241–258, http://dx.doi.org/10.1109/TEVC.2011.2173577.

[52] K. Deb, An introduction to genetic algorithms, Sadhana 24 (4) (1999) 293–315, http://dx.doi.org/10.1007/BF02823145.

[53] L. Casalino, D. Pastrone, Optimization of hybrid propellant mars ascent vehicle, in: 50th AIAA/ASME/SAE/ASEE Joint Propulsion Conference, Cleveland, OH, USA, 2014, http://dx.doi.org/10.2514/6.2014-3953.

[54] L. Casalino, F. Masseni, D. Pastrone, Optimal design of electrically fed hybrid mars ascent vehicle, Aerospace 8 (7) (2021) http://dx.doi.org/10.3390/aerospace8070181.

[55] M. Fabiani, M.T. Migliorino, D. Bianchi, F. Nasuti, M. Franco, F. Barato, N. Bellomo, D. Pavarin, et al., Modeling of swirl injection effects in a H2O2-HDPE hybrid rocket, in: Aerospace Europe Conference-10th EUCASS-9th CEAS, Lausanne, Switzerland, 2023, http://dx.doi.org/10.13009/EUCASS2023-606.

[56] G. Whittinghill, I. Whittinghill, C. Aumann, N. Mosser, Mars ascent vehicle hybrid motor development testing, in: IEEE Aerospace Conference, Big Sky, MT, USA, 2019, pp. 1–8, http://dx.doi.org/10.1109/AERO.2019.8742093.